RESEARCH ARTICLE

Key Points:
- Seafloor heat flow measurements in a spreading center axial valley
- Possible evidence for vigorous hydrothermal circulation cells within upper crust
- Large area of near-zero heat flow with isolated high heat flow hot spots

Quantitative estimate of heat flow from a mid-ocean ridge axial valley, Raven field, Juan de Fuca Ridge: Observations and inferences

Marie S. Salmi[1], H. Paul Johnson[1], Maurice A. Tivey[2], and Michael Hutnak[3]

[1]School of Oceanography, University of Washington, Seattle, Washington, USA, [2]Department of Geology and Geophysics, Woods Hole Oceanographic Institution, Woods Hole, Massachusetts, USA, [3]Earth and Planetary Science, University of California, Santa Cruz, California, USA

Abstract A systematic heat flow survey using thermal blankets within the Endeavour segment of the Juan de Fuca Ridge axial valley provides quantitative estimates of the magnitude and distribution of conductive heat flow at a mid-ocean ridge, with the goal of testing current models of hydrothermal circulation present within newly formed oceanic crust. Thermal blankets were deployed covering an area of 700 by 450 m in the Raven Hydrothermal vent field area located 400 m north of the Main Endeavour hydrothermal field. A total of 176 successful blanket deployment sites measured heat flow values that ranged from 0 to 31 W m^{-2}. Approximately 53% of the sites recorded values lower than 100 mW m^{-2}, suggesting large areas of seawater recharge and advective extraction of lithospheric heat. High heat flow values were concentrated around relatively small "hot spots." Integration of heat flow values over the Raven survey area gives an estimate of conductive heat output of 0.3 MW, an average of 0.95 W m^{-2}, over the survey area. Fluid circulation cell dimensions and scaling equations allow calculation of a Rayleigh number of approximately 700 in Layer 2A. The close proximity of high and low heat flow areas, coupled with previous estimates of surficial seafloor permeability, argues for the presence of small-scale hydrothermal fluid circulation cells within the high-porosity uppermost crustal layer of the axial seafloor.

1. Introduction

Hydrothermal circulation transfers heat from newly formed oceanic crust into the overlying ocean, removing more than 88% of the total heat of formation from crust younger than 1 Ma [*Stein and Stein*, 1994]. The resulting interaction during this transfer of fluid and heat influences the chemical composition of the ocean crust and seawater and establishes an environment for unique chemosynthetic biological communities [*Luther et al.*, 2001].

Most models of hydrothermal circulation geometry for mid-ocean spreading centers are constrained by boundary conditions derived from seismic studies, chemical sampling, and visual observations at high-temperature discharge sites. These indirect data form the basis for a range of models that attempt to quantify hydrothermal circulation within axial ridges and have provided first-order estimates of critical parameters such as permeability, porosity, topography, and heat sources that influence this circulation. It has been suggested that hydrothermal fluid circulation pathways utilize both high-permeability fault zones [*Rabinowicz et al.*, 1999; *Tivey and Johnson*, 2002; *Coumou et al.*, 2008; *Anderson et al.*, 2012; *Lowell et al.*, 2013], as well as more general regions of localized and diffuse matrix permeability [*Davis et al.*, 1997]. Previous models for multiple circulation patterns have included large-scale ridge circulation [*Wilcock*, 1998], slot convection within open fissures [*Delaney et al.*, 1997; *Rabinowicz et al.*, 1999], double-loop single-pass convection [*Lowell et al.*, 2012], and annular convection cells centered on discharge sites [*Coumou et al.*, 2008]. It is probable that more than one of these circulation cell distributions may be present within the same region of an axial valley [*Johnson et al.*, 2010; *Lowell et al.*, 2012].

The heat budget of a spreading ridge depends on factors that include Axial Magma Chamber (AMC) size, depth and location, magma replenishment budget, spreading rate, distribution of faults within the overlying reservoir lid, and the presence or absence of a sealing sediment cover [*Lister*, 1980; *Schultz et al.*, 1992; *Chen and Phipps Morgan*, 1996; *Baker et al.*, 1996]. An unsettled question pertaining to ridge crest hydrothermal circulation is how effectively this process removes heat directly above a heat source, specifically the cooling
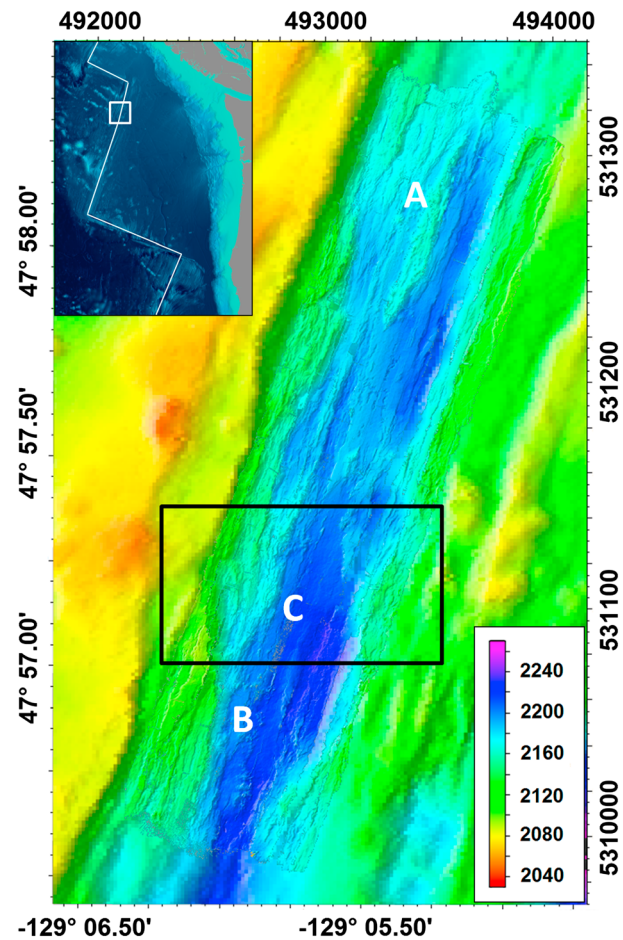
Figure 1. Composite bathymetry map of Endeavour Ridge rift valley showing the location of high-temperature hydrothermal fields (a) High Rise Hydrothermal field, (b) Main Endeavour Hydrothermal field, and (c) the Raven Hydrothermal Field with study area outlined in black. Inset shows location map of the study area within the Endeavour segment (white box) on the Juan de Fuca spreading ridge located off Washington, USA (white line shows plate boundary).

of a shallow magma chamber beneath an axial spreading ridge. Heat flow measured using "bare rock" thermal blankets survey provides a means to identify the hydrothermal circulation pathways within an unsedimented spreading valley.

Heat flow measurements are a reliable proxy for subsurface fluid circulation [*Stein and Stein*, 1992] and have been used to constrain numerical models of fluid flow through the crust in off-axis sedimented regions [*Spinelli and Fisher*, 2004; *Davis et al.*, 2004; *Hutnak et al.*, 2006; *Hutnak and Fisher*, 2007]. The heat flow profiles around active vent sites in Middle Valley on the northern Juan de Fuca ridge provide a first-order understanding of circulation within a fully sedimented spreading center [*Davis and Villinger*, 1992; *Stein et al.*, 1998; *Stein and Fisher*, 2001]. These in situ heat flow measurements have quantified the amount of heat released into the ocean from active high-temperature hydrothermal sites along a sedimented spreading ridge. However, similar high-resolution heat flow data have not been previously available for unsedimented spreading centers.

1.1. The Main Endeavour Ridge Segment

The Endeavour Segment is one of the seven major ridge partitions along the Juan de Fuca mid-ocean ridge that spreads at an intermediate full rate of 5.6–5.7 cm/yr [*Wilson*, 1993] and hosts several large hydrothermal vent fields, the largest being the Main Endeavour Field (MEF) [*Delaney et al.*, 1997; *Kelley et al.*, 2012]. The smaller Raven Hydrothermal Field (maximum vent temperature near 200°C: Figure 1) was initially discovered during remotely operated vehicle (ROV) Jason II surveys in 2000 and 2001 [*Johnson et al.*, 2002] and is located approximately 400 m north of Main Endeavour and 1800 m south of High Rise Field, two of the most active fluid emission sites on the Endeavour Segment [*Kelley et al.*, 2012]. Similar to the Main Endeavour Field, the Raven field lies within a region of reduced crustal magnetization (i.e., a magnetic burnhole) [*Johnson et al.*, 2002; *Tivey and Johnson*, 2002; *Tivey et al.*, 2014]. This association with the hydrothermal fluid emission site suggests that the upper crust in these areas has been chemically and thermally altered by hydrothermal fluids [e.g. *Tivey and Dyment*, 2010]. No vent fluid chemistry has been collected from Raven hydrothermal vents, and the emitted fluid is chemically uncharacterized.

The geological structure of the Main Endeavour/Raven area axial valley consists of major normal faults forming steep boundary walls ~200 m tall on either side of a 300 m wide valley floor. In the subsurface, seismic data resolve a shallow magma chamber approximately 0.8 km wide with a tilted roof 2.1 km below the seafloor on the western side of the valley that deepens to 2.5 km below the eastern edge of the valley [*Van Ark et al.*, 2007].

The eastern flank of the Main Endeavour ridge segment has been the location of several previous heat flow studies [*Davis and Lister*, 1977; *Davis et al.*, 1999; *Wheat et al.*, 2004; *Pribnow et al.*, 2000; *Stein et al.*, 1998; *Hutnak et al.*, 2006]. Within the Endeavour axial valley, a previous low-resolution heat flow survey was centered on the MEF [*Johnson et al.*, 2010]. Studies of hydrothermal plumes overlying the valley have used
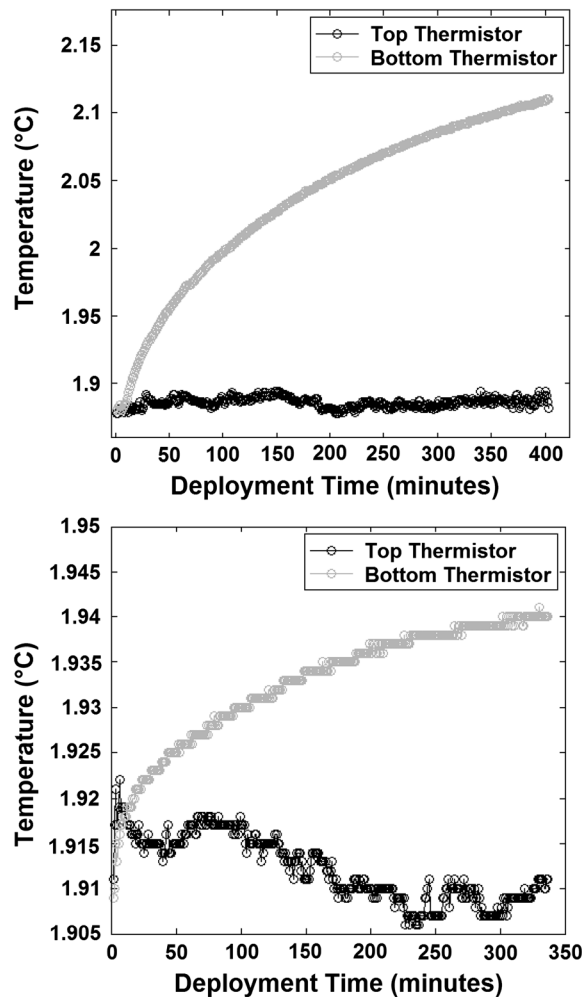
Figure 2. Two examples of blanket deployments used in this analysis. Light grey is the bottom-sealed thermistor, and black is the top thermistor recording bottom water variability. (top) A well-behaved high heat flow example. (bottom) A lower heat flow example with variable bottom water temperature.

conductivity-temperature-depth sensors on ROVs and Autonomous Underwater Vehicles that provide water column estimates of heat issuing from the vent fields, including MEF [*Bemis et al.*, 1993; *Veirs et al.*, 2006; *Baker*, 2007, and references therein; *Kellogg and McDuff*, 2010]. Using the previously developed thermal blanket instrumentation [*Johnson and Hutnak*, 1997], this study deployed a systematic grid of heat flow stations in areas of partial sediment cover (submeter-scale thickness) around the Raven Hydrothermal Field. The goal of this study was to quantify the conductive heat output and characterize hydrothermal circulation pathways within a thermally active spreading center valley.

2. Methods

2.1. Thermal Blankets

To better determine heat flow in regions of sparse sediment cover, data processing methodology for the thermal blankets was improved from the previous method described in *Johnson et al.* [2010]. While the physical configuration of the thermal blankets is unchanged, the postprocessing techniques have been substantially modified to produce more accurate heat flow measurements. The primary improvement consisted of correcting for bottom water temperature variations during deployment periods by using a general Finite Difference Model (FDM) [*Beardsmore and Cull*, 2001] (see supporting information).

Thermal blankets function as sensors by propagating the thermal gradient from the underlying rock into a material matrix of known thermal conductivity (λ_m, in units of W m^{-1} K^{-1}) over a fixed thickness (z), resulting in an internal thermal gradient from T_0 to T_1 therefore allowing for an estimation of heat flow, q (W m^{-2}) using Fourier's Law:

$$q = \lambda_m \frac{T_1 - T_0}{z} \tag{1}$$

The thermal blanket consists of a disk-shaped layer of open cell foam approximately 0.5 m in diameter and 5 cm thick encased in a thin low-permeability fabric shell as described in *Johnson et al.* [2010]. The thermal gradient within the blanket is measured using two Antares thermistors with a resolution of ± 0.001°C located on the top and bottom of the blanket midway across the diameter. Immediately after being placed on the seafloor, the bottom thermistor records an increase in temperature (Figure 2) which will eventually reach a stable value, T_0, depending on the underlying geothermal gradient. The top thermistor records the time-dependent bottom water temperature directly above the blanket, which is used to correct for thermal variations within the blanket. Due to the small size, thermal blankets are easily manipulated using the ROV Jason II, allowing for multiple station deployments for each instrument during a single dive.

Following the removal of external thermal influences with the FDM algorithm (Figure 3), the solution to the heat transfer equation for an infinite half slab was used to determine the evolution of the thermal gradient
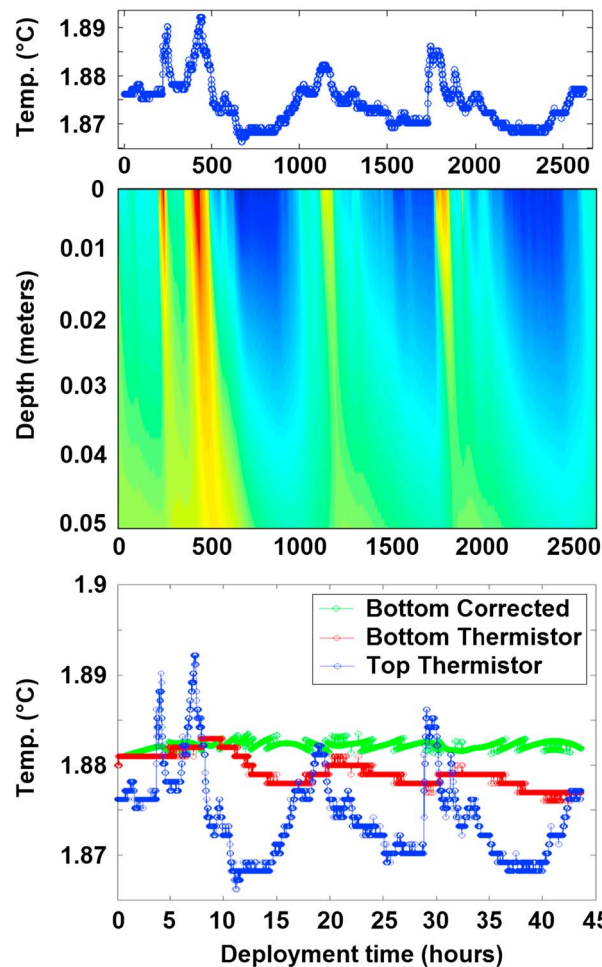
Figure 3. Example of bottom water variations being removed from a thermal blanket deployment. (top) The top thermistor record is incorporated into (middle) the finite difference model as the top boundary condition, resulting in estimated variations recorded by the bottom thermistor caused by temperature anomalies. (bottom) This anomaly can be removed from the bottom thermistor (red) resulting in a record of the corrected heat flow (green).

within the thermal blankets over the deployment period [Carslaw and Jaeger, 1959] (Figure 4). The assumption of infinite half-space does not include edge effects, which were assumed to be negligible for the high aspect ratio of the 2 mm diameter thermistor sensors located at the center of the 0.5 m diameter blanket. In equation (2), T is the temperature based on the variables t (time in seconds) and z (thickness in meters) ranging from initial temperature T_0 to final T_1, with a fixed thermal diffusivity (α) derived from the physical properties of the blanket foam:

$$T(z,t) = T_0 + (T_1 - T_0)\mathrm{erfc}\left(\frac{z}{2\sqrt{\alpha t}}\right) \quad (2)$$

Thermal diffusivity is defined by

$$\alpha = \frac{\lambda_m}{\rho C_p} \quad (3)$$

where C_p is specific heat capacity ($\mathrm{J\,kg^{-1}\,K^{-1}}$), λ_m is the thermal conductivity, and ρ ($\mathrm{kg\,m^{-3}}$) is seawater density. The heat capacity and density used were $3.992 \times 10^{-3}\,\mathrm{J\,kg^{-1}\,K^{-1}}$ and $1039\,\mathrm{kg\,m^{-3}}$ based on a temperature of 2°C and water depth of 2000 m.

The resulting curve produced by this equation was fitted to the bottom thermistor temperature profile by varying the thermal conductivity (λ_m) and the final temperature (T_1) until the best fit or highest r^2 value was determined (Figure 4). The final temperature (T_1) was assumed to be independent of the error function term at $t = \infty$ and is the only parameter used in further analysis. Heat flow was then calculated using Fourier's Law and the estimated parameters λ_m, ΔT (the difference between background water temperature and T_1), and thickness (z).

2.1.1. Thermal Blanket Error

The primary source of a failed thermal blanket deployment resulted when the blanket did not form a complete seal with the seafloor and was therefore unable to record a stable geothermal gradient. These failed stations were readily identified by high-frequency temperature fluctuations visible in the bottom thermistor records that could not be attributed to bottom water temperature variations propagating downward through the blanket. Even a small gap between blanket and seafloor will cause a large disturbance in the thermal gradient, and all stations with signs of a poor seal were discarded and not considered in our postcruise analysis.

Multiple components of the thermal blanket deployment will add to the error in the final estimate of heat flow. One process easily quantified is the propagated error from the resolution of the Antares thermistors. Postprocessing is done by fitting a continuous temperature equation to a data set with a resolution of ±0.001°C, providing noise to the data sets. For high heat flow values, the error associated with thermistor resolution is small but can be substantially larger for low heat flow sites. At a thermal conductivity of $0.56\,\mathrm{W\,m^{-1}\,K^{-1}}$ (at water of 2°C and 2600 m depth), the analog to digital conversion limit of 1 millidegree C will produce an error of $\pm0.011\,\mathrm{W\,m^{-2}}$.
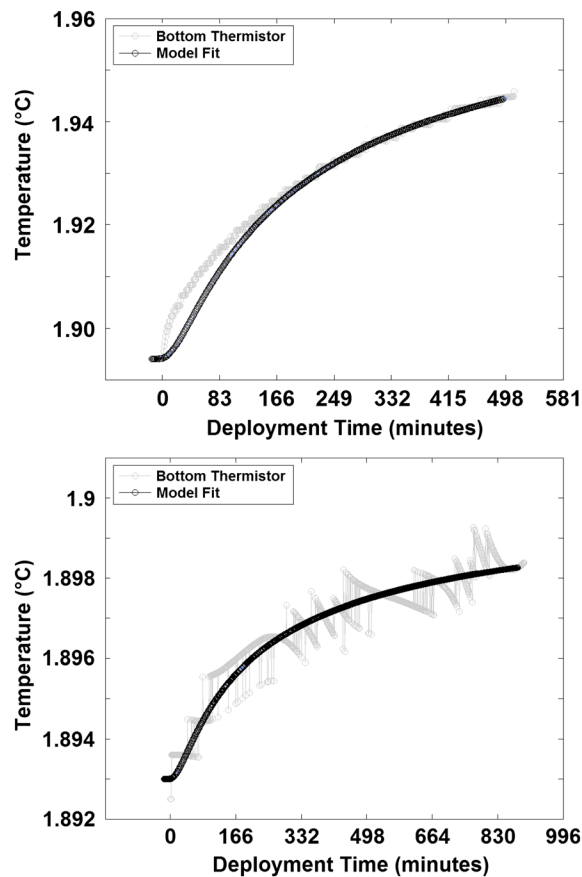
Figure 4. Examples of (top) a warm and (bottom) a cool station fitted to the solution of the infinite half-space heat equation (black line). The light grey line is the resulting bottom thermistor data following the removal of the bottom water variations via the finite difference model.

Variations in substrate thermal conductivity, such as moving from sediment to basalt, could have a minor impact on blanket heat flow by altering the bottom equilibrium temperature (T_1). Due to the FDM construction, these variations were accounted for during the deployment period. Thermal diffusivity variations associated with sediment ($4 \times 10^{-7} \, m^2 \, s^{-1}$) or basalt ($2.5 \times 10^{-7} \, m^2 \, s^{-1}$) sea floor substrate [*Goto and Matsubayashi*, 2009] resulted in minimal variations in blanket thermal heat flow of $\pm 0.0002 \, W \, m^{-2}$. Any cracks or fissures in the basalt/sediment cover or unexpected fluid circulation pathways that would increase thermal diffusivity would result in obvious blanket-failure-to-seal behavior and were thus discarded.

Based on equation (2), the temperature recorded by the thermal blanket bottom thermistor should take ~6.7 days to reach 90% of T_1 (equilibrium) and 27 days to reach 95% of T_1. Basalt has a higher thermal diffusivity than sediment, producing shorter equilibrium times. While this model provides the best fit of the observed thermal blanket parameters, it assumes no fluid circulation (purely conductive) in either blanket or seafloor and does not account for the minimal thermal conductivity changes due to any time-dependent substrate properties. However, there may be minor fluid circulation occurring within the blanket foam matrix at high heat flow values ($>500 \, mW \, m^{-2}$) that would reduce the time to equilibrium but introduce error. Our processing methodology does not, however, require that the blanket reach thermal equilibrium. Possible error in equilibrium temperature estimations (T_1) due to the blanket not reaching equilibrium during the deployment period are accounted for by how well the data fit theoretical modeled behavior (see supporting information).

Prior to a blanket deployment, bottom water temperature variability can alter the thermal environment within the near-seafloor substrate. A temperature mooring (i.e., NE Mooring) connected to the Neptune Canada fiber optic cabled observatory [Ocean Networks Canada Data Archive, 2014, http://www.oceannetworks.ca] recorded long-term background temperature variability within the axial valley away from any high-temperature vent system. Bottom water temperature data for the Endeavour axial valley recorded 6 months prior to and including the blanket survey period ranged from 1.85°C to 1.92°C. Downward propagation of this temperature variation [*Hamamoto et al.*, 2005] using a thermal diffusivity of $4 \times 10^{-7} \, m^2 \, s^{-1}$ results in a temperature variation range of $\pm 0.02°C$ at 1 m and ~0.002°C at 3 m depth below the seafloor. This could result in a possible heat flow error with a standard deviation of $\pm 15 \, mW \, m^{-2}$ over several months.

2.2. Raven Heat Flow Survey

The heat flow survey presented in this paper includes data derived from 13 individual thermal blankets, each deployed at multiple stations using the ROV Jason II during a 2011 R/V *Atlantis* cruise (AT18-09). During this cruise, Jason conducted two 48 h dives for a total bottom time of 96 h, collecting measurements at 192 thermal blanket stations. Of this number, 16 stations were not processed because of failure to seal on the seafloor, leaving 176 successful blanket deployments. Most blankets were deployed in a quasi-systematic grid
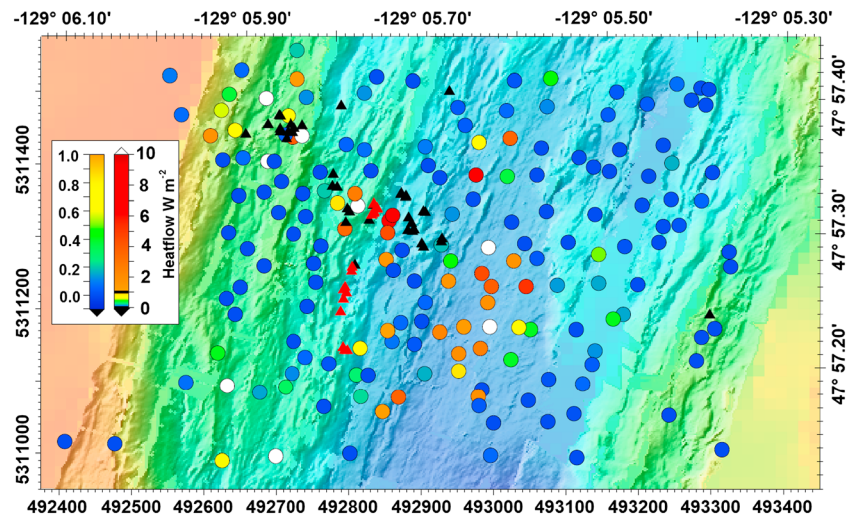
Figure 5. Measured heat flow values (filled circles) overlaid on 1 m resolution SM2000 directionally shaded bathymetry. Red triangles are active hydrothermal venting locations. Black triangles are remanent dead sulfide stacks.

with an average spacing of 50 m over a rectangular area 700 by 450 m. An additional eight deployments extended westward over the western rift valley wall, approaching the first off-axis sedimented valley. Also included in this data set are 10 previous heat flow stations on an E-W profile between the Raven and MEF in 2003 [*Johnson et al.*, 2010], located less than 100 m from the southern boundary of the 2011 Raven survey. These data were reprocessed using the current methodology described above and extended the heat flow survey area by 100 m southward.

Thermal blankets could not be deployed over a small section near the eastern axial valley wall due to the presence of large talus fields that would have prevented blankets from sealing properly. A smaller area on the western axial valley wall was also not sampled due to the active hydrothermal venting and sulfide debris located along the normal fault near the intersection with the valley floor and talus fields.

Any blanket showing a negative heat flow value after processing, where the top thermistor had a warmer temperature than the bottom thermistor, was assigned a value of $0.0\,W\,m^{-2}$. In these cases, the assumption was made that the actual geothermal gradient was extremely low and the top thermistor was registering localized warming of the overlying water column due to currents within the axial valley [*Hautala et al.*, 2012].

2.3. Two-Dimensional Interpolation of Heat Flow Over the Valley Floor

To aid in interpretation and areal pattern recognition, surface interpolation of the final processed heat flow data used the geostatistical method Simple Kriging. This method was implemented using the Geostatistical Analysis component within the Environmental Systems Research Institute (ESRI) ArcGIS software package [*Environmental Systems Research Institute*, 2011]. Heat flow values were interpolated using a Gaussian and linear model, assuming a known stationary mean. This resulted in the lowest residual fit to the data, producing a generalized interpolation that accounts for the spatial variability and the ability to resolve moderate length scale patterns within the discrete heat flow measurement grid.

3. Results

Heat flow measurements ranged between 0 and $30\,W\,m^{-2}$ with the majority of the stations only slightly above $0.0\,W\,m^{-2}$. Overall, 59% of heat flow values ranged between 0.0 and $0.1\,W\,m^{-2}$ and slightly more than half of those (69 stations) recorded values at or below $0.0\,W\,m^{-2}$. Ten stations exceeded $10\,W\,m^{-2}$, with one station reaching $30.5\,W\,m^{-2}$ (Figure 5).

Stations that are classified as "cool" ($<0.1\,W\,m^{-2}$) occupy much of the axial valley floor and walls. Heat flow exceed the $+0.1\,W\,m^{-2}$ threshold only at localized hot spots and were located primarily on the western rift valley wall and within the central valley. No heat flow values above $1.0\,W\,m^{-2}$ were detected along the eastern valley wall (Figures 5 and 6). Hot spot areas on the western wall were linearly distributed along azimuth 130°,
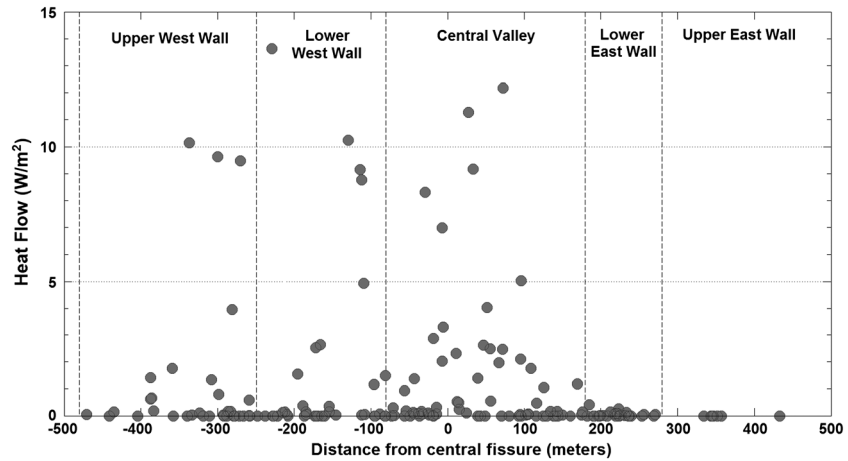
Figure 6. Measured heat flow data projected onto a plane perpendicular to the spreading ridge-strike-centered around the prominent fault within the western valley. Included within this profile are heat flow stations collected during the 2011 survey (this paper) and the "north line" from the 2003 Main Endeavour heat flow survey [*Johnson et al.*, 2010].

a direction offset ~20° from orthogonal to the azimuth of the west wall (N020°) (Figure 5). Two additional warm values of >10 W m^{-2} formed a localized hot spot in the southwestern corner of the survey area. Hot spots located within the axial valley floor were composed of larger areas of relatively high heat flow compared to the smaller, more localized distribution of high-temperature stations identified on the west wall (Figure 5).

Large differences in heat flow were found between stations located in close proximity to each other, strongly suggesting that the thermal anomalies are produced by sources in the shallow subsurface. The most extreme example of large horizontal differences in heat flow are two blankets located on the upper west wall near universal transverse mercator (UTM) coordinates: 49,270 Northing, 5,311,400 Easting, near a cluster of dead sulfide structures, which had a difference in heat flow values of 10 W m^{-2} and were located only 20 m apart
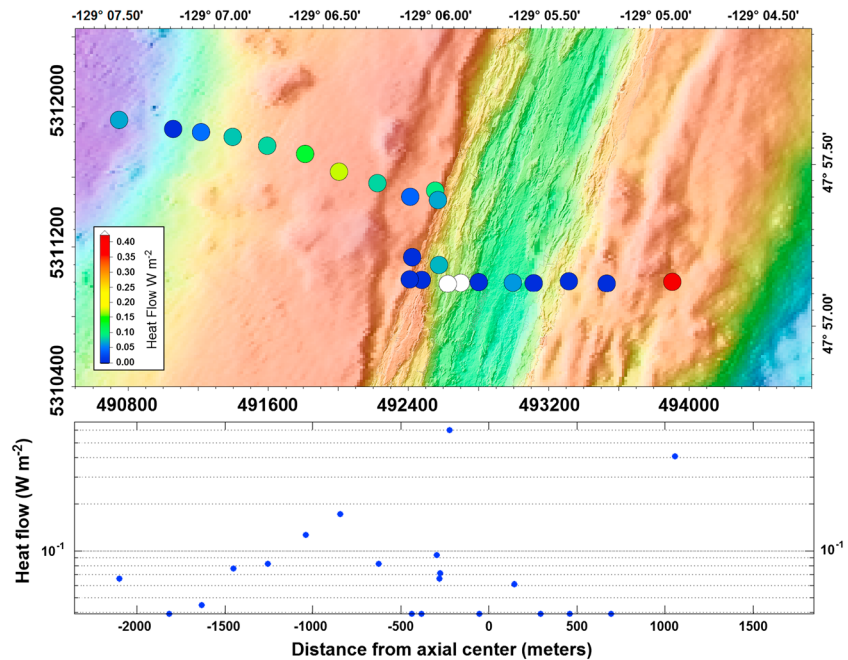

Figure 7. Heat flow profile over the west and east walls providing a more complete heat flow profile transecting the axial ridge and rift valley. Profile includes heat flow stations over the west wall collected during the 2011 survey (this paper) and the north line from the 2003 Main Endeavour heat flow survey [*Johnson et al.*, 2010].
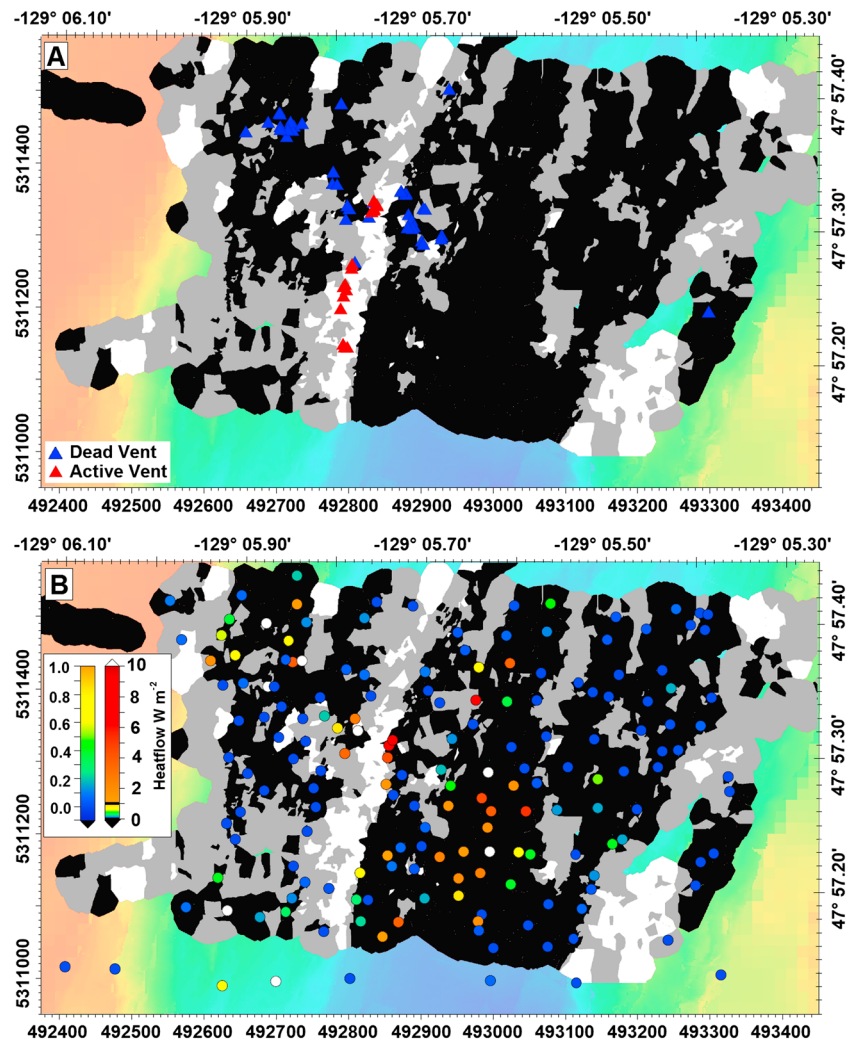
Figure 8. ROV image-derived surface permeability (adapted from *Hearn et al.* [2013]). Black corresponds to low permeability associated with full sediment cover, while white corresponds to high permeability related to loose rubble/talus.

(Figure 5). This pattern of large variation in heat flow measurements between proximal sites appears in several other locations within the survey site, including west of the active Raven hydrothermal vents, within the axial valley floor and near the dead sulfide deposits on the west wall (Figure 5).

In addition to the dense grid of stations located within the axial valley, heat flow values were also obtained over the western ridge flank. Combined with 10 blanket stations from a 2003 cruise [*Johnson et al.*, 2010], these stations outside the valley walls provide an E-W cross-axis heat flow profile of the axial valley and flanks (Figure 7). Heat flow along this transect ranges from zero to 12 W m^{-2} and gradually increases over the west ridge flank, peaking near the summit and then decreasing to zero W m^{-2} within the axial valley, except at the previously discussed localized hot spots. This off-axis cooling trend continues symmetrically up the eastern wall, with the exception of one warm location within an intensively faulted region at the top of the eastern ridge flank (Figure 7).

3.1. Heat Flow Versus Surface Permeability

ROV Jason video-frame-grab images have been used to estimate surface permeability for the same Raven area as the heat flow study (Figure 8) [*Hearn et al.*, 2013]. In that study, surface permeability was classified as high, medium, or low based on semiquantitative visual observations of seafloor sediment cover, exposed rock type, and fissure density. In addition to surface permeability, *Hearn et al.* [2013] identified the locations of both active venting sites and inactive sulfide deposits, where the latter were interpreted as locations of
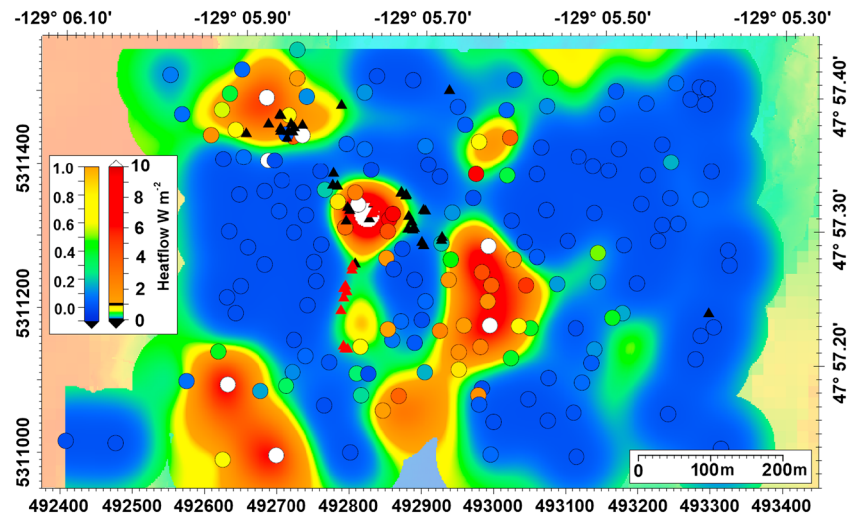
Figure 9. Surface interpolation of heat flow stations using the Simple Kriging methodology overlain by measured heat flow values (filled circles).

previous hydrothermal fluid discharge (Figure 8a). Most of the inactive sulfide deposits are located along the western side of the axial valley, continue up the western wall, and are associated with moderate to high heat flow values within areas of low and medium seafloor permeability. The only high-surface permeability areas of this study are associated with regions of the western wall that hosts the presently active fluid discharge sites, suggesting a strong positive correlation that appears to be causal (Figure 8a).

The localized hot spot at the intersection of the along-ridge trend of active vents and the across-strike linear distribution of inactive sulfide deposits appears within a region of predominantly medium- and high-surface permeability seafloor (Figures 5 and 8). It is important to note that the remaining high heat flow "hot spots" within the axial valley are located within the axial valley floor (Figure 8b), which consists largely of low-permeability areas that are almost completely covered with sediment and appear to be unbroken sheet flows except for a few visibly open fissures.

3.2. Heat Flow Interpolation

The interpolation "reach" for the Simple Kriging models applied to the high-quality sites was between 75 and 120 m and provides a generalized fit that describes spatial heat flow patterns encompassing both distant and localized hot spot distribution. The Kriging error of $\pm 0.9\,\mathrm{W\,m^{-2}}$ is caused by large variations in measurements obtained between sites that were in close spatial proximity to each other within the high heat flow locations. Due to the nominal 50 m spacing of the thermal blanket sites, it was not possible to resolve features smaller than this length scale.

Assuming that surface interpolation accurately reflects the conductive heat flow distribution, the resulting Kriging model was resampled into $1\,\mathrm{m^2}$ cells for visual display (Figure 9). The total heat output from this survey site can be estimated by integrating the heat flow from each cell over the entire survey area. This calculation results in a total conductive heat output for the Raven Hydrothermal Field study area of 0.3 MW or an average heat flow of $0.95\,\mathrm{W\,m^{-2}}$.

4. Discussion

This high-resolution heat flow survey of a relatively unsedimented but active hydrothermal region presents a uniquely detailed picture of heat distribution within an intermediate spreading mid-ocean ridge axial valley. A similar conductive heat flow experiment was previously conducted within the Main Endeavour axial valley [*Johnson et al.*, 2010], but at a much lower spatial resolution and without bottom water temperature corrections. Spacing between heat flow stations limits our general ability to quantify higher-order spatial variations, as illustrated by stations with large contrasting heat flow values in very close proximity (Figure 5). However, spatial variations within our survey grid can resolve 50–200 m length scale patterns that identify

both individual hot spots and cold seafloor potentially indicative of seafloor recharge. These data provide strong evidence of active hydrothermal circulation cells occurring within the uppermost igneous crustal basement of the axial valley floor.

The presence of large areas of near-zero surface heat flow also implies shallow (within the top several hundred meters of Layer 2A) and vigorous hydrothermal circulation capable of transferring large amounts of heat from an underlying magma chamber. Measurements made in the presence of downward fluid pressure gradients (i.e., recharge locations) are known to show suppressed heat flow in the surrounding seafloor [*Stein et al.*, 1998]. Expanded areas of potential recharge zones may represent hydrothermal circulation that occurs on a larger scale than the Raven area alone. These may be associated with the much larger high-temperature axial vent fields located to the north and south of this survey site [*Kelley et al.*, 2012].

Based on both actual station measurements and the data interpolation, localized hot spots distributed near the west valley wall are small, well defined, and are in sharp contrast to the colder surrounding seafloor. This differs from the high heat flow hot spots within the axial valley floor that appear less well defined and more broadly distributed than those along the western wall. This dissimilarity in the two areas can be explained by spatial differences in the depth of water penetration into the subsurface prior to returning to the seafloor. The hot spots located on the western wall are spatially correlated with the high-temperature fluid discharge that produces sulfide deposits and circulation in these discharge areas appear fault controlled. Faults can provide spatial stability through time compared to more mobile cells located beneath the porous axial valley floor. One of the inactive sulfide deposits near a Raven west wall hot spot has been recently dated as approximately 2000 years in age, [*Jamieson et al.*, 2013], supporting the view that the hot spots associated with high-temperature emissions and sulfide deposits may be relatively long lived features.

In contrast to the actively venting sites, the linear across-strike distribution of relic fluid emission sites identified by inactive sulfide deposits extending up the western valley wall (Figure 5) is not correlated with any visible surface expression of faulting, although there is considerable talus cover over much of the area. This is different from the presently active vent areas, which are associated with the large ridge-strike-oriented normal faults that are clearly visible to the ROV video cameras. These observations suggest that currently active fluid discharge sites may be correlated with subsurface faults that extend deeper than the uppermost Layer 2A crustal section. An ocean bottom seismometer (OBS) grid previously deployed in this area detected earthquakes that switch along strike from thrust faults to normal faulting within the crust immediately above the AMC approximately 100 m north of the Raven area [*Wilcock et al.*, 2009]. This seismic transition zone in fault mode is oriented parallel to the linear trend connecting the heat flow hot spots and inactive dead sulfide deposits up the west wall. Finally, high-resolution magnetics [*Tivey et al.*, 2014] also show a similar southeast to northwest trend in reduced magnetization that correlate with the heat flow values, sulfide deposit distribution, and seismic structure. These correlations in azimuthal trends within the same portion of the axial valley are unlikely to be a coincidence and strongly suggest deeper E-W structural control on the high-temperature fluid pathways (Figure 5).

4.1. Ridge-Scale Circulation

Our measurements of conductive heat flow, extending as profiles over both the west and east flanks of the axial ridge, provide insight into these larger-scale crustal circulation patterns. Generalized areas of cold seafloor surrounding localized high-temperature vent sites within the axial valley lend support to the near-field toroidal-shaped pathway model of *Coumou et al.* [2008] where cold seawater flows into the axial valley subsurface crust and recharges both shallow (< 500 m) and deep (> 1 km) hydrothermal cells within the axial valley (Figures 5 and 7). In addition, based on the areal distribution of increased heat flow near the apex of the valley flanking ridges, off-axis fluid upwelling, and likely low levels of fluid emission may also occur along the thinly sedimented western ridge flank summit.

This pattern of topographic forcing of shallow fluid circulation by abyssal ridges outside the axial valley is consistent with previous results [*Fisher et al.*, 1990; *Johnson et al.*, 1993; *Fisher and Becker*, 1995; *Wang et al.*, 1997; *Hutnak et al.*, 2008; *Fisher and Harris*, 2010]. *Johnson et al.* [1993] used the Alvin heat flow probe to determine heat flow west of Main Endeavour but were unable to make measurements over the axial ridge and axial valley due to a lack of sediment thickness required for conventional heat flow probe measurements. The present thermal blanket profile over the western axial ridge flank now completes this
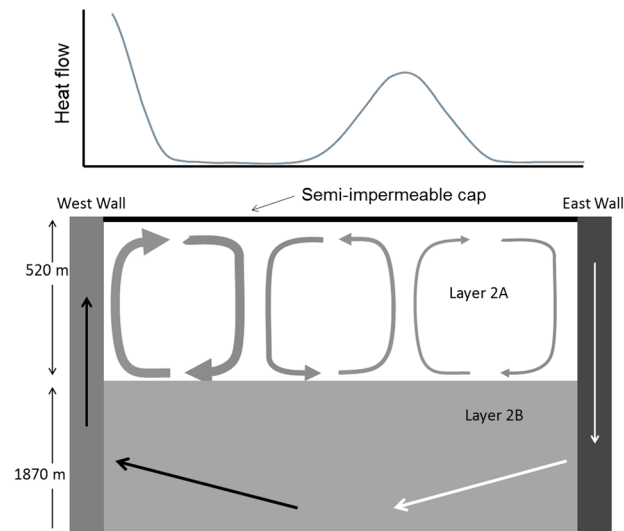
Figure 10. The proposed 2-D circulation model within the Layer 2A assuming large deep hydrothermal circulation with recharge along the east wall and discharge along the west wall due to a tilted axial magma chamber. Low porosity within Layer 2A may allow for the formation of localized circulation cells.

earlier profile (Figure 7) and demonstrates that topographically forced crustal fluid circulation clearly continues within the poorly sedimented ridge that flanks the axial valley and exchanges heat between the upper crustal rocks and seawater.

4.2. Shallow Circulation Within the Axial Valley

The presence of tightly constrained zones of altered upper crust associated with hydrothermal fluid emission sites has been previously observed using crustal magnetization, water temperature, and conductive heat flow data [*Johnson et al.*, 1982; *Tivey and Johnson*, 2002; *Johnson et al.*, 2010]. In addition to these observations, numerical models have also predicted annular recharge zones encircling centralized areas of fluid discharge with isotropic permeability structures [*Coumou et al.*, 2008]. The close spacing of ~100 m between conductive hot spots within areas of mostly impermeable seafloor (Figure 8) now also suggests the presence of relatively small shallow fluid circulation cells located within the first few hundred meters of the upper Layer 2A of the oceanic crust. The general concept of shallow fluid circulation cells located within the upper crust has been previously suggested by *Alt* [1995], *Delaney et al.* [1997], *Wilcock* [1998], *Tivey and Johnson* [2002], *Kelley et al.* [2002], and *Lowell et al.* [2007], and this model appears to be supported by our present conductive heat flow survey (Figure 5).

4.3. Hydrothermal Model

A proposed hydrothermal circulation conceptual model that explains the heat flow measurements on the valley floor and lower valley walls is shown in Figure 10. In this model, seawater enters the extrusive igneous (pillow basalt) rock matrix that forms the upper Layer 2A via cracks, fissures, and faults in areas adjacent to discharge sites and in more distal regions of the axial valley, particularly the eastern valley wall. Previous near-bottom gravity data have been used to estimate a porosity of 30% for the upper crustal Layer 2A [*Holmes and Johnson*, 1993; *Pruis and Johnson*, 1998; *Cochran et al.*, 1999; *Johnson et al.*, 2000] and specifically for the axial valley at Endeavour [*Gilbert and Johnson*, 1999]. This high porosity is further supported by the low seismic velocities determined from MCS and OBS seismic work in the area [*Newman et al.*, 2011; *Weekly et al.*, 2014]. For our model below, we assume a transition zone between Layers 2A and 2B that is based on the well-defined seismic velocity structure of *Van Ark et al.* [2007].

The influx of cold seawater into the upper crustal reservoir produces large areas of low heat flow, specifically on the eastern side of the valley. Low values of conductive heat flow $<10\,\mathrm{mW\,m^{-2}}$ are highly anomalous compared to the estimated conductive average heat flow of $\sim 1\,\mathrm{W\,m^{-2}}$ for an axial spreading center [*Stein and Stein*, 1992]. This background heat flow can be estimated using equation (1) with an assumed thermal conductivity (λ_m) of $2\,\mathrm{W\,m^{-1}\,K^{-1}}$ [*Lowell and Germanovich*, 2004; *Spinelli and Fisher*, 2004], a thermal gradient of 1198°C ($T_0 = 1$°C and $T_1 = 1200$°C), and a depth (z) of 2300 m to the AMC. The across-axis hydrothermal circulation shown in Figure 10 has been suggested to be driven by the nonuniform depth of the top of the underlying magma chamber that shoals to the west and deepens to the east [*Johnson et al.*, 2010]. This cross-axis east-to-west fluid circulation is also believed to be the dominant fluid circulation pathway at MEF located 500 m to the south of the Raven survey area [*Johnson et al.*, 2010; *Tivey and Johnson*, 2002]. At MEF, cold seawater is heated by interactions with the hot rock lying just above the melt zone, producing the high-temperature fluids. These fluids then move upward in a narrow high-permeability upflow zone from deep within Layer 2B, forming the active high-temperature vent sites found along the west wall [*Kelley et al.*, 2002].

Away from the valley walls, the presence of localized hot spots within areas of impermeable unbroken sheet flows and near 100% sediment cover (Figures 8 and 9) strongly suggests an additional mode of hydrothermal circulation occurs within the uppermost crust of Layer 2A. High-temperature fluid emissions on the lower west wall consist of hot hydrothermal fluids originating from deep within Layer 2B. These higher temperatures at the top of Layer 2B also provide the heat that drives a secondary pattern of shallow circulation cells within the porous Layer 2A. This two-layered circulation model, consisting of a deep (Layer 2B) system that interacts with high-temperature basalt near the AMC and shallow circulation pathways constrained completely within Layer 2A, is similar to a model previously suggested by *Lowell et al.* [2012]. Smaller circulation cells would be constrained within Layer 2A, bounded below by the lower permeability of Layer 2B and above by the semi-impermeable surface of mostly unbroken seafloor lithology and sediment cover [*Hearn et al.*, 2013]. Active fluid circulation within Layer 2A would increase the effective thermal conductivity and reduce the thermal gradient of the uppermost crust, as discussed below. This distribution of temperatures in discrete vertical layers, from a high of 350–550°C for the deep layer to a cooler 100–200°C for the shallow layer, has been previously suggested for the Gorda Ridge [*Hart et al.*, 1990].

To test the plausibility of this model of small circulation cells contained within the uppermost crust, we need to first examine if fluid circulation cells can exist within the matrix of Layer 2A. That is accomplished by estimating the Rayleigh number (*Ra*) for the system using equations from *Lowell and Germanovich* [2004] for constant heat flow scaling, which we believe is physically more realistic than the alternative model of assuming a constant ΔT for the upper and lower boundaries of Layer 2A. Using the scaling relationships from *Lowell and Germanovich* [2004], the horizontal distances between hot spots can be linked to underlying circulation paths by the scale analysis result

$$L \sim hRa^{-1/4} \tag{4}$$

The thickness of Layer 2A in this segment of the spreading center, *h*, is estimated to be 520 m based on the seismic study of *Van Ark et al.* [2007]. The value for *L* is assumed to be 100 m, based on the Kriging heat flow map (Figure 9).

The resulting Rayleigh number (*Ra*) calculated using the parameters derived above is approximately 700 and is clearly in excess of the critical Rayleigh number, which ranges from 17.7 to 27.1 [*Nield*, 1968; *Tan et al.*, 2003], strongly supporting vigorous hydrothermal circulation within the 2A layer. This value only estimates the vigor of potential fluid circulation and ignores the presence of faults and anisotropy within the upper crustal section. This high *Ra* number reinforces the model of shallow crustal circulation cells being responsible for the localized patterns of seafloor heat flow identified by our thermal blanket survey.

5. Conclusions

Quantitative heat flow measurements determined using thermal blankets over the Raven Hydrothermal Field on the Juan de Fuca spreading ridge provide valuable insight into hydrothermal circulation within very young crust. Conductive heat flow was measured over an area of 450×700 m and identified large regions of near-zero heat flow adjacent to high heat flow hot spots, which were located primarily along the western valley wall and within the central axial valley. This pattern for shallow fluid circulation within Layer 2B is compatible with an additional deeper, across-axis hydrothermal circulation of high-temperature fluid flowing from east to west within uppermost Layer 2B [*Johnson et al.*, 2010].

Regions of high heat flow surround both active and inactive sulfide deposits, suggesting that "dead" hydrothermal vent sites that appear visually to be inactive may be continuing to host low-temperature diffuse fluid flow or residual heat that is difficult to detect directly. Active high-temperature discharge sites are distributed along a large prominent fault running along the base of the west valley wall and parallel to the ridge axis. Dead sulfide deposits appear to form a linear trend across the rift valley and west wall that is oriented almost perpendicular to the strike of the spreading axis. This inactive sulfide deposit alignment is parallel to, and located near, a previously identified seismic transition zone in crustal structure, which suggests deeper crustal control on the high-temperature fluid circulation [*Wilcock et al.*, 2009].

Patterns of thermally driven fluid circulation within the deeper crust include both rift valley wall-to-wall circulation beneath the axial valley floor, and secondary small circulation cells present entirely within shallow Layer 2A. These shallow circulation cells are identified by the sharp transitions between hot spots and the large areas of near-zero heat flow ($0.0 \, W \, m^{-2}$). Finally, a Raleigh number for Layer 2A of 700 supports the proposed conceptual model of small multipass circulation cells present within the uppermost igneous crust.

References

Alt, J. C. (1995), Subseafloor processes in mid-ocean ridge hydrothermal systems, in *Seafloor Hydrothermal Systems: Physical, Chemical, Biological, and Geological Interactions, Geophys. Monogr. Ser.*, vol. 91, edited by S. E. Humphris et al., pp. 85–114, AGU, Washington, D. C.

Anderson, B. W., L. A. Coogan, and K. M. Gillis (2012), The role of outcrop-to-outcrop fluid flow in off-axis oceanic hydrothermal systems under abyssal sedimentation conditions, *J. Geophys. Res.*, *117*, B05103, doi:10.1029/2011JB009052.

Baker, E. (2007), Hydrothermal cooling of mid-ocean ridge axes: Do measured and modeled heat flows agree?, *Earth Planet. Sci. Lett.*, *263*, 140–150.

Baker, E. T., Y. J. Chen, and J. Phipps Morgan (1996), The relationship between near-axis hydrothermal cooling and the spreading rate of mid-ocean ridges, *Earth Planet. Sci. Lett.*, *142*, 137–145.

Beardsmore, G. R., and J. P. Cull (2001), *Crustal Heat Flow. A Guide to Measurement and Modelling*, 324 pp., Cambridge Univ. Press, Cambridge, U. K.

Bemis, K. G., R. P. Von Herzen, and M. J. Mottl (1993), Geothermal heat flow from hydrothermal plumes on the Juan de Fuca Ridge, *J. Geophys. Res.*, *98*, 6351–6365, doi:10.1029/92JB02273.

Carslaw, H. S., and J. C. Jaeger (1959), *Conduction of Heat in Solids*, 2nd ed., 510 pp., Oxford Univ. Press, New York.

Chen, Y. J., and J. Phipps Morgan (1996), The effects of spreading rate, the magma budget, and the geometry of magma emplacement on the axial heat flow at mid-ocean ridges, *J. Geophys. Res.*, *101*, 11,475–11,482, doi:10.1029/96JB00330.

Cochran, J. R., D. J. Fornari, B. J. Coakley, R. Herr, and M. A. Tivey (1999), Continuous near-bottom gravity measurements made with a BGM-3 gravimeter in DSV Alvin on the East Pacific Rise crest near 9° 31′ N and 9° 50′ N, *J. Geophys. Res.*, *104*(B5), 10,841–10,861, doi:10.1029/1999JB900049.

Coumou, D., T. Driesner, and C. A. Heinrich (2008), The structure and dynamics of mid-ocean ridge hydrothermal systems, *Science*, *321*, 1825–1828.

Davis, E. E., and C. R. B. Lister (1977), Heat flow measured over the Juan de Fuca Ridge: Evidence for widespread hydrothermal circulation in a highly heat transportive crust, *J. Geophys. Res.*, *82*, 4845–4860, doi:10.1029/JB082i030p04845.

Davis, E. E., and H. Villinger (1992), Tectonic and thermal structure of the Middle Valley sedimented rift, northern Juan de Fuca Ridge, in *Proc. ODP, Init. Repts.*, vol. 139, edited by E. E. Davis et al., pp. 9–41, Ocean Drilling Program, College Station, Tex., doi:10.2973/odp.proc.ir.139.102.

Davis, E. E., H. Villinger, and A. Rosenberger (1997), An unequivocal case for high Nusselt number hydrothermal convection in sediment-buried igneous oceanic crust, *Earth Planet. Sci. Lett.*, *146*, 137–150.

Davis, E. E., et al. (1999), Regional heat flow variations across the sedimented Juan de Fuca Ridge eastern flank: Constraints on lithospheric cooling and lateral hydrothermal heat transport, *J. Geophys. Res.*, *104*, 17,675–17,688, doi:10.1029/1999JB900124.

Davis, E. E., K. Becker, and J. He (2004), Costa Rica Rift revisited: Constraints on shallow and deep hydrothermal circulation in young oceanic crust, *Earth Planet. Sci. Lett.*, *222*, 863–879.

Delaney, J. R., D. S. Kelley, M. D. Lilley, D. A. Butterfield, R. E. McDuff, J. A. Baross, J. W. Deming, H. P. Johnson, and V. Robigou (1997), The Endeavour hydrothermal system: Part I, Cellular circulation above an active cracking front yields large sulfide structures, "fresh" vent water, and hyperthermophile archaea, *RIDGE Events*, *8*, 11–19.

Environmental Systems Research Institute (2011), *ArcGIS Desktop: Release 10*, Environmental Systems Research Institute, Redlands, Calif.

Fisher, A. T., and K. Becker (1995), Correlation between seafloor heat flow and basement relief: Observational and numerical examples and implications for upper crustal permeability, *J. Geophys. Res.*, *100*(B7), 12,641–12,657, doi:10.1029/95JB00315.

Fisher, A. T., and R. N. Harris (2010), Using seafloor heat flow as a tracer to map subseafloor fluid flow in the ocean crust, *Geofluids*, *10*, 142–160, doi:10.1111/j.1468-8123.2009.00274.x.

Fisher, A. T., K. Becker, T. N. Narismhan, M. G. Langseth, and M. J. Mottl (1990), Passive, off-axis convection through the southern flank of the Costa Rica Rift, *J. Geophys. Res.*, *95*, 9343–9370, doi:10.1029/JB095iB06p09343.

Gilbert, L. A., and H. P. Johnson (1999), Direct measurements of oceanic crustal density at the northern Juan de Fuca Ridge, *Geophys. Res. Lett.*, *26*, 3633–3636, doi:10.1029/1999GL008391.

Goto, S., and O. Matsubayashi (2009), Relations between the thermal properties and porosity of sediments in the eastern flank of the Juan de Fuca Ridge, *Earth Planets Space*, *61*, 863–870.

Hamamoto, H., M. Yamano, and S. Goto (2005), Heat flow measurement in shallow seas through long-term temperature monitoring, *Geophys. Res. Lett.*, *32*, L21311, doi:10.1029/2005GL024138.

Hart, R., J. Hoefs, and D. Pyle (1990), Gorda Ridge: A seafloor spreading center in the United States' Exclusive Economic Zone, in *Proceedings of the Gorda Ridge Symposium*, edited by G. R. McMurray, pp. 51–75, Springer, New York, Portland, Ore.

Hautala, S., H. P. Johnson, M. Pruis, I. Garcia-Berdeal, and T. Bjorklund (2012), Low-temperature hydrothermal plumes in the near-bottom boundary layer at Endeavour Segment, Juan de Fuca Ridge, *Oceanography*, *25*, 192–196.

Hearn, C. K., K. L. Homola, and H. Paul Johnson (2013), Surficial permeability of the axial valley seafloor: Endeavour Segment, Juan de Fuca Ridge, *Geochem. Geophys. Geosyst.*, *14*, 3409–3424, doi:10.1002/ggge.20209.

Holmes, M. L., and H. P. Johnson (1993), Upper crustal densities derived from sea floor gravity measurements: Northern Juan de Fuca Ridge, *Geophys. Res. Lett.*, *20*(17), 1871–1874, doi:10.1029/93GL00909.

Hutnak, M., and A. T. Fisher (2007), The influence of sedimentation, local and regional hydrothermal circulation, and thermal rebound on measurements of heat flux from young seafloor, *J. Geophys. Res.*, *112*, B12101, doi:10.1029/2007JB005022.

Hutnak, M., A. T. Fisher, L. Zuhlsdorff, V. Spiess, P. H. Stauffer, and C. W. Gable (2006), Hydrothermal recharge and discharge guided by basement outcrops on 0.7–3.6 Ma seafloor east of the Juan de Fuca Ridge: Observations and numerical models, *Geochem. Geophys. Geosyst.*, *7*, Q07O02, doi:10.1029/2006GC001242.

Hutnak, M., A. T. Fisher, R. Harris, C. Stein, K. Wang, G. Spinelli, M. Schindler, H. Villinger, and E. Silver (2008), Large heat and fluid fluxes driven through mid-plate outcrops on ocean crust, *Nat. Geosci.*, *1*, 611–614.

Jamieson, J. W., M. D. Hannington, D. A. Clague, D. S. Kelley, J. R. Delaney, J. F. Holden, M. K. Tivey, and L. E. Kimpe (2013), Sulfide geochronology along the Endeavour Segment of the Juan de Fuca Ridge, *Geochem. Geophys. Geosyst.*, *14*, 2084–2099, doi:10.1002/ggge.20133.

Johnson, H. P., and M. Hutnak (1997), Conductive heat loss in recent eruptions at mid-ocean ridges, *Geophys. Res. Lett.*, *24*, 3089–3092, doi:10.1029/97GL02998.

Johnson, H. P., J. L. Karsten, F. J. Vine, and G. C. Smith (1982), A low level magnetic survey over a massive sulfide ore body in the Troodos ophiolite complex, Cyprus, *Mar. Technol. Soc. J.*, *16*(3), 76–80.

Johnson, H. P., K. Becker, and R. P. Von Herzen (1993), Near-axis heat flow measurements on the northern Juan de Fuca Ridge, *Geophys. Res. Lett.*, *20*, 1875–1878, doi:10.1029/93GL00734.

Johnson, H. P., M. J. Pruis, D. Van Patten, and M. A. Tivey (2000), Density and porosity of the upper oceanic crust from seafloor gravity measurements, *Geophys. Res. Lett.*, *27*, 1053–1056, doi:10.1029/1999GL011130.

Johnson, H. P., et al. (2002), Survey studies hydrothermal circulation on the northern Juan de Fuca Ridge, *Eos Trans. AGU*, *83*, 73–79, doi:10.1029/2002EO000043.

Johnson, H. P., M. A. Tivey, T. A. Bjorklund, and M. S. Salmi (2010), Hydrothermal circulation within the Endeavour Segment; Juan de Fuca Ridge, *Geochem. Geophys. Geosyst.*, *11*, Q05002, doi:10.1029/2009GC002957.

Kelley, D. S., J. A. Baross, and J. R. Delaney (2002), Volcanoes, fluids, and life at mid-ocean ridge spreading centers, *Annu. Rev. Earth Planet. Sci.*, *30*, 385–491.

Kelley, D. S., et al. (2012), Endeavour Segment of the Juan de Fuca Ridge: One of the most remarkable places on Earth, *Oceanography*, *25*, 44–61.

Kellogg, J. P., and R. E. McDuff (2010), A hydrographic transient above the Salty Dawg hydrothermal field, Endeavour Segment, Juan de Fuca Ridge, *Geochem. Geophys. Geosyst.*, *11*, Q12001, doi:10.1029/2010GC003299.

Lister, C. R. B. (1980), Heat flow and hydrothermal circulation, *Annu. Rev. Earth Planet. Sci.*, *8*, 95–117.

Lowell, R. P., and L. N. Germanovich (2004), Hydrothermal processes at mid-ocean ridges: Results from scale analysis and single-pass models, in *Mid-Ocean Ridges: Hydrothermal Interaction Between the Lithosphere and Ocean*, pp. 219–244, AGU, Washington, D. C.

Lowell, R. P., S. Gosnell, and Y. Yang (2007), Numerical simulations of single-pass hydrothermal convection at mid-ocean ridges: Effects of the extrusive layer and temperature-dependent permeability, *Geochem. Geophys. Geosyst.*, *8*, Q10011, doi:10.1029/2007GC001653.

Lowell, R. P., A. Farough, L. N. Germanovich, L. B. Hebert, and R. Horne (2012), A vent-field-scale model of the East Pacific Rise 9°50′N magma-hydrothermal system, *Oceanography*, *25*, 158–167.

Lowell, R. P., A. Farough, J. Hoover, and K. Cummings (2013), Characteristics of magma-driven hydrothermal systems at oceanic spreading centers, *Geochem. Geophys. Geosyst.*, *14*, 1756–1770, doi:10.1002/ggg.20109.

Luther, G. W., T. F. Rozan, M. Taillefert, D. B. Nuzzio, C. Di Meo, T. M. Shank, R. A. Lutz, and S. C. Cary (2001), Chemical speciation drives hydrothermal vent ecology, *Nature*, *410*, 813–6.

Newman, K. R., M. R. Nedimović, J. P. Canales, and S. M. Carbotte (2011), Evolution of seismic layer 2B across the Juan de Fuca Ridge from hydrophone streamer 2-D travel time tomography, *Geochem. Geophys. Geosyst.*, *12*, Q05009, doi:10.1029/2010GC003462.

Nield, D. (1968), Onset of thermohaline convection in a porous medium, *Water Resour. Res.*, *4*, 553–560, doi:10.1029/WR004i003p00553.

Ocean Networks Canada Data Archive (2014), http://www.oceannetworks.ca, Oceans Networks Canada, University of Victoria, Canada.

Pribnow, D. F. C., E. E. Davis, and A. T. Fisher (2000), Borehole heat flow along the eastern flank of the Juan de Fuca Ridge, including effects of anisotropy and temperature dependence of sediment thermal conductivity, *J. Geophys. Res.*, *105*, 13,449–13,456, doi:10.1029/2000JB900005.

Pruis, M. J., and H. P. Johnson (1998), Porosity of very young oceanic crust from sea floor gravity measurements, *Geophys. Res. Lett.*, *25*(11), 1959–1962, doi:10.1029/98GL01412.

Rabinowicz, M., J.-C. Sempéré, and P. Genthon (1999), Thermal convection in a vertical permeable slot: Implications for hydrothermal circulation along mid-ocean ridges, *J. Geophys. Res.*, *104*, 29,275–29,292, doi:10.1029/1999JB900259.

Schultz, A., J. R. Delaney, and R. E. McDuff (1992), On the partitioning of heat flow between diffuse and point source seafloor venting vent, *J. Geophys. Res.*, *97*, 12,299–12,314, doi:10.1029/92JB00889.

Spinelli, G. A., and A. T. Fisher (2004), Hydrothermal circulation within topographically rough basaltic basement on the Juan de Fuca Ridge flank, *Geochem. Geophys. Geosyst.*, *5*, Q02001, doi:10.1029/2003GC000616.

Stein, J. S., and A. T. Fisher (2001), Multiple scales of hydrothermal circulation in Middle Valley, northern Juan de Fuca Ridge: Physical constraints and geologic models, *J. Geophys. Res.*, *106*, 8563–8580, doi:10.1029/2000JB900395.

Stein, C. A., and S. Stein (1992), A Model for the global variation in oceanic depth and heat flow with lithospheric age, *Nature*, *359*, 123–129.

Stein, C. A., and S. Stein (1994), Constraints on hydrothermal heat flow through the oceanic lithosphere from global heat flow, *J. Geophys. Res.*, *99*, 3081–3095, doi:10.1029/93JB02222.

Stein, J. S., A. T. Fisher, M. Langseth, W. Jin, G. Iturrino, and E. E. Davis (1998), Fine-scale heat flow, shallow heat sources, and decoupled circulation systems at two sea-floor hydrothermal sites, Middle Valley, northern Juan de Fuca Ridge, *Geology*, *26*, 1115–1118.

Tan, K., T. Sam, and H. Jamaludin (2003), The onset of transient convection in bottom heated porous media, *Int. J. Heat Mass Transf.*, *46*, 2857–2873.

Tivey, M. A., and J. Dyment (2010), The magnetic signature of hydrothermal systems in slow spreading environments, in *Diversity of Hydrothermal Systems on Slow Spreading Ridges*, *Geophys. Monogr. Ser.*, edited by P. A. Rona et al., pp. 43–65, AGU, Washington, D. C., doi:10.1029/2008GM000773.

Tivey, M. A., and H. P. Johnson (2002), Crustal magnetization reveals subsurface structure of Juan de Fuca Ridge hydrothermal vent fields, *Geology*, *30*, 979–982.

Tivey, M. A., H. P. Johnson, M. S. Salmi, and M. H. Hutnak (2014), High-resolution near-bottom vector magnetic anomalies over Raven Hydrothermal Field, Endeavour Segment, Juan de Fuca Ridge, *J. Geophys. Res. Solid Earth*, doi:10.1002/2014JB011223.

Van Ark, E. M., R. S. Detrick, J. P. Canales, S. M. Carbotte, A. J. Harding, G. M. Kent, M. R. Nedimovic, W. S. D. Wilcock, J. B. Diebold, and J. M. Babcock (2007), Seismic structure of the Endeavour Segment, Juan de Fuca Ridge: Correlations with seismicity and hydrothermal activity, *J. Geophys. Res.*, *112*, B02401, doi:10.1029/2005JB004210.

Veirs, S. R., R. E. McDuff, and F. R. Stahr (2006), Magnitude and variance of near-bottom horizontal heat flow at the Main Endeavour hydrothermal vent field, *Geochem. Geophys. Geosyst.*, *7*, Q02004, doi:10.1029/2005GC000952.

Wang, K., J. He, and E. E. Davis (1997), Influence of basement topography on hydrothermal circulation in sediment-buried igneous oceanic crust, *Earth Planet. Sci. Lett.*, *46*, 151–164.

Weekly, R. T., W. S. D. Wilcock, D. R. Toomey, E. E. E. Hooft, and E. Kim (2014), Upper crustal seismic structure of the Endeavour Segment, Juan de Fuca Ridge from travel time tomography: Implications for oceanic crustal accretion, *Geochem. Geophys. Geosyst.*, *15*, 1296–1315, doi:10.1002/2013GC005159.

Wheat, C. G., M. J. Mottl, A. T. Fisher, D. Kadko, E. E. Davis, and E. Baker (2004), Heat flow through a basaltic outcrop on a sedimented young ridge flank, *Geochem. Geophys. Geosyst.*, *5*, Q12006, doi:10.1029/2004GC000700.

Wilcock, W. S. D. (1998), Cellular convection models of mid-ocean ridge hydrothermal circulation and the temperatures of black smoker fluid, *J. Geophys. Res.*, *103*, 2585–2596, doi:10.1029/97JB03252.

Wilcock, W. S. D., E. E. E. Hooft, D. R. Toomey, P. R. McGill, A. H. Barclay, D. S. Stakes, and T. M. Ramirez (2009), The role of magma injection in localizing black-smoker activity, *Nat. Geosci.*, *2*, 509–513.

Wilson, D. S. (1993), Confidence intervals for motion and deformation of the Juan de Fuca Plate, *J. Geophys. Res.*, *98*, 16,053–16,071, doi:10.1029/93JB01227.